Robust Sahel drought due to the Interdecadal Pacific Oscillation in CMIP5 simulations.

Julián Villamayor[1] and Elsa Mohino[2]

Affiliation:

[1,2]Departamento de Física de la Tierra, Astronomía y Astrofísica I, Universidad Complutense de Madrid, Madrid, Spain.

Contact:

[1]Av. Complutense s/n, 28040 Madrid, Spain. julian.villamayor@fis.ucm.es

[2]Av. Complutense s/n, 28040 Madrid, Spain. emohino@fis.ucm.es

Abstract:

Many studies address the Interdecadal Pacific Oscillation (IPO) as a modulator of climate in several regions all over the globe. However very few suggest it has an impact on Sahel rainfall low-frequency variability. This work shows the relevance of such connection, supported by a robust response of state-of-the-art global climate models. Our results reveal that the positive phase of the IPO has a negative impact on Sahel rainfall anomalies regardless of the externally forced changes induced by anthropogenic gases. Such relationship is stronger for those models in which sea surface temperatures associated with the positive phase of the IPO show warmer anomalies over the Tropical Pacific. Therefore, we suggest the importance of a skillful simulation of IPO to improve decadal prediction of Sahel rainfall and to better understand its variability.

1. Introduction:

The Interdecadal Pacific Oscillation (IPO) is a low-frequency mode of variability usually defined as the leading empirical orthogonal function (EOF) of the detrended sea surface temperature anomalies (SSTA) over the Pacific basin at decadal timescales (Figures 1a and 1b) [Zhang et al., 1997; Power et al., 1999]. The IPO is the basin-wide manifestation of the Pacific Decadal Oscillation (PDO), which is defined as the leading EOF of North Pacific detrended SSTA in winter [Mantua et al., 1997]. During its positive (negative) phase, the IPO sea surface temperature (SST) pattern is characterized by warm (cold) anomalies in the tropics and cold (warm) ones over the central and western extratropical Pacific (Figure 1b) [Trenberth and Hurrell, 1994; Meehl et al., 2009]. The origin of the mode is still under discussion. Some works suggest that it can arise by noise [Newman et al., 2003; Schneider and Cornuelle 2005; Shakun and Shaman, 2009], while others argue that the IPO is produced by atmosphere-ocean interactions involving the tropics and the extratropics [Deser et al., 2004; Meehl and Hu, 2006; Farneti et al., 2014]. Due to its vast temperature signal in the tropical Pacific, the IPO can offset or intensify the warming of globally averaged surface air temperatures [Gu and Adler, 2013; Meehl et al., 2013]. The IPO also impacts precipitation. It has been associated with drought conditions over the northern hemisphere summer monsoon [Hwang et al., 2013] and particularly over North America [Meehl and Hu, 2006; Dai, 2013] and in the Indian monsoon [Krishnan and Sugi, 2003; Meehl and Hu, 2006]; and has been shown to modulate the teleconnections of El Niño Southern Oscillation (ENSO) with rainfall over Australia [Power et al., 1999; Arblaster et al., 2002].

The Sahel is a semiarid region in West Africa extending between the humid savanna south of 10ºN and the beginning of the Sahara Desert at roughly 18ºN. The majority of the annual precipitation takes place in the boreal summer season, from July to September (JAS), and it is linked to the West African monsoon [Sultan and Janicot, 2003; Losada et al., 2010; Nicholson et al., 2013]. Due to the socio-economic importance of water resources in the region, the Sahel is highly vulnerable to rainfall variability. Throughout the 20th Century, Sahel precipitation has shown strong variability at decadal timescales [Mohino et al., 2011a]. Especially relevant was the prolonged period of drought in the 1970s and 1980s, which draw the attention of many studies [e.g. Folland et al., 1986; Giannini et al., 2003; Dai et al., 2004; Caminade and Terray, 2010; Mohino et al., 2011a; Rodríguez-Fonseca et al., 2011]. There is currently a broad agreement that the main driver of Sahel precipitation at decadal timescales is SST variability amplified by land-surface processes [Zeng et al., 1999; Giannini et al., 2003; Kucharski et al., 2013].

Sahel rainfall variability is influenced by SST anomalies over different regions at multiple timescales. At interannual timescales, a warming of the equatorial Atlantic and ENSO-like SST anomalies over the Indo-Pacific promote drought over the Sahel [Janicot, 2001; Vizy and Cook, 2002; Giannini et al., 2005; Cook and Vizy, 2006; Joly and Voldoire, 2009; Mohino et al., 2011b; Losada et al., 2010, among others], while warmer conditions over the Mediterranean sea are linked to enhanced Sahel rainfall (Rowell, 2003). At decadal timescales, many works have highlighted the influence of the Atlantic Multidecadal Oscillation (AMO) on Sahel precipitation [e.g. Zhang and Delworth, 2006; Hoerling et al. 2006; Knight et al., 2006; Ting et al., 2009, 2011, 2014; Mohino et al., 2011a; Martin et al. 2014]. However, up to now, the few studies that have been done on the possible impact of the IPO on Sahel rainfall have shown a negative correlation (Figure 1c) [Joly, 2008; Mohino et al., 2011a] and a possible modulation of the effect of ENSO due to the IPO [Molion and Lucio, 2013].

In this study, we investigate the impact of the IPO on Sahel precipitation using the simulations from the Coupled Model Intercomparison Project – Phase V (CMIP5) [Taylor et al., 2012]. We particularly address the following questions: (1) Is there an impact of the IPO on Sahel precipitation? (2) What is the dynamical mechanism for such impact? (3) How do coupled models simulate the IPO and its impact over the Sahel? (4) Does the radiative forcing affect this relationship?

2. Data and Methods:

We work with monthly data of SST, precipitation and wind at high (200 hPa.) and low (850 hPa.) levels. To analyze the observed IPO and impacts we use HadISST1 [Rayner et al., 2003] and ERSSTv3 [Smith et al., 2008] SST reconstructions, CRUTS3.1 precipitation [Mitchel and Jones, 2005] and winds from the 20th Century Reanalysis [Compo et al., 2011]. For the simulations, the output from 17 different CMIP5 models is used, previously interpolated to a common regular grid with a spatial resolution of 2.8º in longitude and latitude. We have analyzed the unforced long-term preindustrial control (piControl) run; the historical run, which is a reproduction of the 20th century (typically from 1850-2005) with observed external forcing imposed; and the rcp8.5 future projection experiment, which considers the highest increase of anthropogenic gases concentration (see detailed list of models and simulations analyzed in Table S1 in the supplementary material).

Depending on the definition, some anthropogenic component can be included in the IPO index [Bonfils and Santer, 2011]. In order to isolate the internal variability of SSTs as much as possible, we remove the global component of the anthropogenic forcing in observations and forced simulations. To do so, we calculate a "residual" field from the annual mean SSTA following Mohino et al. [2011a]: We define a global warming (GW) index as the lowpass-filtered (40-yr cutoff) time series of averaged SSTA between 45ºS and 60ºN. We regress the original SSTA onto the GW index and we construct a "GW fitted" SSTA field by multiplying the regression coefficient at each grid point by the GW index. Finally, we subtract the "GW fitted" SSTA field from the original one and obtain the "residual" SSTA field. To focus on decadal timescales, the "residual" field is lowpass-filtered (13-yr cutoff).

The IPO indices from observations and the forced simulations (historical and rcp8.5 experiments) are then defined as the first principal component (PC) of the "residual" SSTA, associated to the first

Empirical Orthogonal Function (EOF) calculated over the Pacific basin (between 60ºN-45ºS). The members of the residual SSTA of the models with several realizations available are concatenated in time before applying the EOF analysis. For the externally unforced piControl simulations the IPO index is defined as the PC associated with the first EOF of the 13-year lowpass-filtered original SSTA field.

Once the IPO index of each model is calculated, the model SST and rainfall patterns are obtained by regressing the unfiltered fields onto the IPO index. To highlight the consistent response from models, the patterns from the 17 models are averaged together. The statistical significance of the averaged patterns is evaluated with a Monte Carlo-based test (see details in supplementary material).

3. Results:

In accordance with previous studies [Mantua et al., 1997; Mantua and Hare, 2002; Deser et al., 2004; Shen et al., 2006; Mohino et al., 2011a; Dai, 2013], the observed IPO index shows cold regimes in the periods of 1909-1925, 1944-1976 and from 1998 onwards, and warm regimes in the periods 1925-1944 and 1976-1998 (Figure 1a). However, such time variability shows no dominant frequency but various spectral peaks at decadal and multidecadal periodicities, mainly in the 15-25 and 50-70 year bands (Figure S1), in accordance with previous works [Minobe, 1999; Chao et al., 2000; Tourre at al., 2001; Mantua and Hare, 2002; MacDonald and Case, 2005]. On average, models tend to show higher power spectra in two frequency bands, one close to 50-70 years and the other one close to 15-25 years (Figure S2). This suggests that, though there is no clear well-defined periodicity for the IPO (in accordance with the proxy reconstruction from Shen et al. [2006]), the power spectra in models and observations tends to cluster around two preferred bands, of approximately 15-25 and 50-70 years.

The SST pattern associated with the IPO in the historical and control simulations is consistent with observations (Figures 2a, 2c and 1b): In the Pacific, there are cold anomalies over the western part of the basin, poleward of 25º and more prominent in the Northern Hemisphere. There are also warm anomalies over the Tropical Pacific, and over the north and south of the eastern part of the basin. Outside the Pacific basin, the models show a less consistent response among themselves and with the observations. There are, however, regions of anomalous warming over the Indian Ocean, the Tropical Atlantic and next to the southeast coast of Brazil in both simulations and in the observations. The agreement among models on the SST pattern associated with the IPO is weaker in the historical runs than in the piControl ones.

Associated with a positive IPO, the models simulate a significant pattern of negative precipitation anomalies across the Sahel (Figures 2b and 2d), in accordance with observations (Figure 1c). Nevertheless, the observed positive anomalies of precipitation on the coastal area of Guinea, Sierra Leone and Liberia are not reproduced in the simulations. Models underestimate the intensity of the precipitation anomalies in comparison to observations (note different scales on Figure 1c and Figures 2b and 2d). Apart from the attenuation produced by the model mean, the individual models also show this underestimation (Figures S5 and S6). Such underestimation of Sahel rainfall is consistent with an underestimated atmospheric response over West Africa at low and middle levels (not shown). We speculate that the origin of the underestimation could be attributed to the weak rainfall response that Atmospheric General Circulation Models forced with prescribed SSTs show over the Sahel at these time scales [e.g. Rodríguez-Fonseca et al., 2011; Joly et al. 2007; Kucharski et al., 2013], and could be related to the accuracy with which the vegetation-atmosphere feedbacks are parameterized [Giannini et al., 2003; Wang et al., 2007]. It should be noted that, despite the high resemblance between the precipitation patterns coming from both experiments, the agreement among models is higher in the piControl run than in the historical one.

Sahel drought in response to the IPO is a remarkably consistent feature across models and simulations (Figure 3a). For both, historical and piControl experiments, 13 out of the 17 models analyzed simulate a negative correlation between the IPO and the unfiltered Sahel precipitation index. The larger correlation coefficients obtained for the observations suggest a stronger relationship in the real world. The scatter plot in Figure 3b shows that the stronger the SSTA warming over the tropical Pacific, the stronger the IPO's impact on Sahel drought. There are, however, a few models (4 out of 17 models in each experiment) that produce a positive impact of the IPO on Sahel rainfall, though most of these impacts are not statistically significant. These models tend to show a poorly defined IPO spatial pattern in the Pacific basin with weak positive or even negative SSTA over the Tropical Pacific (inmcm4 and MRI-CGCM3 for the historical simulation and GISS-E2-H and GISS-E2-R for the piControl one; Figures S3 and S4). However, some models with a weak or even positive Sahel rainfall response to IPO show warm SSTA over the Tropical Pacific (for instance the CSIRO-Mk3-6-0 model in both experiments; Figures S3 and S4). The positive SSTA over the northeastern Tropical Atlantic basin, with comparable magnitude to the ones over the Pacific warm tongue could partly explain this behaviour (Figures S3 and S4). Such northeastern Tropical Atlantic SSTA has been shown to promote increased rainfall over Sahel [Cook and Vizy, 2006; Giannini et al., 2013] and could be overriding the Tropical Pacific influence in some cases. When both regions, Tropical Pacific and northeastern Tropical Atlantic (boxed areas in Figures 2a), are used to calculate the scatter plot (Figure S7), the explained inter-model variance increases from 0.26 to 0.33, which suggests that a strong negative Sahel precipitation response to IPO is linked to a strong warming over the Tropical Pacific and weak anomalies over the Tropical North Atlantic (Figure 3b).

In observations and simulations, a positive IPO is associated with anomalous convergence over the central Tropical Pacific and divergence over the Tropical Atlantic and West Africa at low levels, and with anomalous divergence and convergence over these two regions, respectively, at high levels (Figure 4). This suggests an anomalous Walker-type overturning cell that connects upward movements over the central Pacific in response to local warm SSTAs there with subsidence over West Africa. This, in turn, reduces the Tropical Easterly Jet and the low-level monsoon westerlies, weakening the monsoon (not shown) and leading to drought conditions over the Sahel. Such mechanism was also proposed for the impact of ENSO events on Sahel rainfall [Janicot, 2001; Joly and Voldoire, 2009; Mohino et al., 2011b]. The similarity between the teleconnection mechanisms at different time scales is consistent with the similar SST patterns over the Tropical Pacific observed for the ENSO and IPO [Deser et al., 2004].

4. Discussion:

The similarity between the SSTA patterns of the historical and the unforced piControl simulations suggests that the IPO SST mode is mainly produced by the internal variability of the models, and that radiative effects do not play a relevant role. However, it is also noticeable that the patterns associated with the IPO are more consistent among models in the piControl experiments than in the historical ones (Figure 2). The methodology we use to obtain the residual SSTA in observations and in the forced runs eliminates the long-term global component of the external forcing. However the external component with more localized effects is not removed. This is especially relevant in the case of aerosols, for which important uncertainties still remain [Boucher et al., 2013]. Such uncertainties could translate into a slightly different behavior of the residual SSTA among models in some regions and, thus, to a less robust SSTA pattern response to IPO in historical simulations than in piControl ones.

Since the models are able to reproduce a modulation of Sahel rainfall by the IPO robustly and congruent to what was observed over the last century, we consider if this relationship will change in the future. The majority of models project an increase of Sahel rainfall for mid- and late 21st century under rcp8.5 scenario, though the presence of outliers and the increase of the inter-model dispersion with time suggest a high degree of uncertainty [Biasutti, 2013; Vizy et al., 2013]. The SSTA IPO pattern for the rcp8.5 simulations is similar to the historical and piControl simulations (Figure 5a). This suggests that under conditions of high anthropogenic gases concentrations, the Pacific internal processes that generate the IPO SST pattern will not be altered. However, the consistency among models is lower than in the other experiments. Difficulties to capture IPO-like SSTA patterns of some models with respect to the other simulations (i.e. bcc-csm1-1, CNRM-CM5, HadGEM2-ES and NorESM1-M) introduce more discrepancies across all models (Figure S9). As in the historical pattern, this may be due to the methodology used to extract the external forcing. Note that the rcp8.5 future projection introduces a stronger radiative forcing and may induce more discrepancies between models when computing the residual SSTA. In addition, the rcp8.5 runs are shorter (typically from 2006-2100, detailed in Table S1) and the IPO-like decadal variability may not be properly captured with an EOF analysis. The impact of the rcp8.5 IPO on rainfall (Figure 5b) is also negative on the Sahel as in the other simulations and it is produced by a similar atmospheric mechanism (Figure S8). Therefore the CMIP5 simulations suggest that the SSTA pattern associated with the IPO variability mode is not expected to change in the future nor its impact on Sahel precipitation.

We must highlight the strong consistency across CMIP5 models found in this work in reproducing the observed IPO modulation of Sahel rainfall low-frequency variability. Conversely, the AMO relationship with Sahel rainfall, which has been broadly studied [e.g. Zhang and Delworth, 2006; Hoerling et al., 2006; Knight et al., 2006; Ting et al., 2009, 2011, 2014; Mohino et al., 2011a], is not as consistently reproduced by CMIP5 models [Martin et al., 2014]. Therefore, although the influence of the AMO is greater than that of the IPO in observations, our results suggest that climate models might not behave in the same way when analyzing the decadal variability of the Sahel rainfall led by modes of SST variability.

5. Summary and conclusions:

In this work we show that most CMIP5 global climate models reproduce a consistent and well-defined IPO SST pattern with a robust negative (positive) impact on Sahel rainfall linked to its positive (negative) phase. This result coincides with observations and supports the hypothesis that the IPO modulates decadal variability of Sahel rainfall through an anomalous Walker-type circulation that produces subsidence over West Africa in the positive phase. The skill of each model to simulate this connection is related to the IPO SSTA pattern. Models reproducing a well-defined Tropical Pacific warm tongue have a significant negative IPO impact on Sahel rainfall, while models with weak Tropical Pacific SSTAs compared to the northeastern Tropical Atlantic ones show a small impact over the Sahel.

The small differences between the IPO SSTA and Sahel rainfall patterns from forced and unforced simulations suggest that the IPO is mainly an internal mode. From our analysis of rcp8.5 future projections we expect that the IPO SST mode and its influence on Sahel rainfall will not change in the future even if there is an increase of anthropogenic gases concentration.

Skill in decadal predictions of Sahel rainfall are model dependent and have been mainly attributed to the skillful reproduction of AMO related SSTs [van Oldenborgh et al., 2012; García-Serrano et al., 2013; Gaetani and Mohino, 2013]. Current GCMs show very low skill in predicting the SST anomalies associated with the IPO [Kim et al., 2012; Doblas-Reyes et al., 2013; Kirtman et al., 2013] and Newman [2013] showed that similar or even better skill could be obtained with a linear inverse model. Our results suggest that an improved characterization of the predicted SSTA pattern and timing of IPO events could be key to enhancing the skill of Sahel rainfall decadal predictions.

6. Acknowledgements:

The authors thank the helpful comments of the two anonymous reviewers and the editor Dr. Diffenbaugh. The research leading to these results has received funding from the European Union Seventh Framework Programme (FP7/2007-2013) under grant agreement n° 603521 and the Spanish project CGL2012-38923-C02-01. We acknowledge the World Climate Research Programme's Working Group on Coupled Modelling, which is responsible for CMIP, and we thank the climate modelling groups for producing and making available their model output. For CMIP the U.S. Department of Energy's Program for Climate Model Diagnosis and Intercomparison provides coordinating support and led development of software infrastructure in partnership with the Global Organization for Earth System Science Portals. Thanks are also given to the MICINN of the Spanish Government for the Scholarship that JV has been granted.

7. References:

Arblaster, J., G. Meehl, and A. Moore (2002), Interdecadal modulation of Australian rainfall, Clim. Dyn., 18(6), 519–531.

Biasutti, M. (2013), Forced Sahel rainfall trends in the CMIP5 archive, J. Geophys. Res. Atmos., 118, 1613–1623, doi:10.1002/jgrd.50206.

Bonfils, C., and B. D. Santer (2011), Investigating the possibility of a human component in various pacific decadal oscillation indices, Clim. Dyn., 37(7–8), 1457–1468.

Boucher, O., D. Randall, P. Artaxo, C. Bretherton, G. Feingold, P. Forster, V. -M. Kerminen, Y. Kondo, H. Liao, U. Lohmann, P. Rasch, S. K. Satheesh, S. Sherwood, B. Stevens and X. Y. Zhang (2013), Clouds and Aerosols, in Climate Change 2013: The Physical Science Basis, Contribution of Working Group I to the Fifth Assessment Report of the Intergovernmental Panel on Climate Change [Stocker, T.F., D. Qin, G.-K. Plattner, M. Tignor, S.K. Allen, J. Boschung, A. Nauels, Y. Xia, V. Bex and P.M. Midgley (eds.)] , pp 571–657, Cambridge University Press, Cambridge, United Kingdom and New York, NY, USA.

Caminade, C., and L. Terray (2010), Twentieth century Sahel rainfall variability as simulated by the ARPEGE AGCM, and future changes, Clim. Dyn., 35, 75–94.

Chao, Y., M. Ghil, and J. C. McWilliams (2000), Pacific interdecadal variability in this century's sea surface temperatures, Geophys. Res. Lett., 27(15), 2261–2264.

Compo, G. P., J. S. Whitaker, P. D. Sardeshmukh, N. Matsui, R. J. Allan, X. Yin, B. E. Gleason, R. S. Vose, G. Rutledge, P. Bessemoulin, S. Brönnimann, M. Brunet, R. I. Crouthamel, A. N. Grant, P. Y. Groisman, P. D. Jones, M. C. Kruk, A. C. Kruger, G. J. Marshall, M. Maugeri, H. Y. Mok, Ø. Nordli, T. F. Ross, R. M. Trigo, X. L. Wang, S. D. Woodruff, and S. J. Worley (2011), The Twentieth Century Reanalysis Project, Q.J.R. Meteorol. Soc., 137, 1–28, doi: 10.1002/qj.776.

Cook, K. H., and E. K. Vizy (2006), Coupled Model Simulations of the West African Monsoon System: Twentieth- and Twenty-First-Century Simulations, J. Clim., 19(15), 3681–3703.

Dai, A., P. J. Lamb, K. E. Trenberth, M. Hulme, P. D. Jones, and P. Xie (2004), The recent Sahel drought is real, Int. J. Climatol., 24, 1323–1331.

Dai, A. (2013), The influence of the inter-decadal Pacific oscillation on US precipitation during 1923–2010, Clim. Dyn., 41(3–4), 633–646.

Deser, C., A. S. Phillips, and J. W. Hurrell (2004), Pacific Interdecadal Climate Variability: Linkages between the Tropics and the North Pacific during Boreal Winter since 1900, Journal of Climate, 17(16), 3109–3124.

Doblas-Reyes, F. J., I. Andreu-Burillo, Y. Chikamoto, J. García-Serrano, V. Guemas, M. Kimoto, T. Mochizuki, L. R. L. Rodrigues, and G. J. van Oldenborgh (2013), Initialized near-term regional climate change prediction, Nature Comms., 4, 1715, doi:10.1038/ncomms2704.

Farneti, R., F. Molteni, and F. Kucharski (2014), Pacific interdecadal variability driven by tropical-extratropical interactions, Clim. Dyn., 42, 11–12, 3337–3355.

Folland, C. K., T. N. Palmer, D. E. Parker (1986), Sahel rainfall and worldwide sea temperatures, 1901-85, Nature, 320, 602–607, doi:10.1038/320602a0.

Gaetani, M., and E. Mohino (2013), Decadal prediction of the Sahelian precipitation in CMIP5 simulations, J. Clim., 26, 7708–7719. doi:10.1175/JCLI-D-12-00635.1.

García-Serrano, J., F. J. Doblas-Reyes, R. J. Haarsma, and I. Polo (2013), Decadal prediction of the dominant West African monsoon rainfall modes, J. Geophys. Res., 118, 5260–5279.

Giannini, A., R. Saravannan, and P. Chang (2003), Oceanic forcing of Sahel rainfall on interannual to interdecadal time scales, Science, 302, 1027–1030.

Giannini A, R. Saravannan, P. Chang (2005), Dynamics of the boreal summer African monsoon in the NSIPP1 atmospheric model, Clim.Dyn., 25:517–535, doi:10.1007/s00382-005–0056.

Giannini, A., S. Salack, T. Lodoun, A. Ali, A. T. Gaye, and O. Ndiaye (2013), A unifying view of climate change in the Sahel linking intra-seasonal, interannual and longer time scales, Environ. Res. Lett., 8, 024010, doi:10.1088/1748-9326/8/2/024010.

Gu, G., and R. F. Adler (2013), Interdecadal variability/long-term changes in global precipitation patterns during the past three decades: global warming and/or pacific decadal variability?, Clim. Dyn., 40(11–12), 3009–3022.

Hoerling, M., J. Hurrell, J. Eischeid, and A. Phillips (2006), Detection and attribution of twentieth-century northern and southern African rainfall change, J. Clim., 19(16), 3989–4008.

Hwang, Y. T., D. M. Frierson, and S. M. Kang (2013), Anthropogenic sulfate aerosol and the southward shift of tropical precipitation in the late 20th century, Geophys. Res. Lett., 40(11), 2845–2850.

Janicot, S., S. Trzaska, and I. Poccard (2001), Summer Sahel-ENSO teleconnection and decadal time scale SST variations, Clim. Dyn., 18(3–4), 303–320.

Joly, M. (2008), Rôle des océans dans la variabilité climatique de la Mousson Africaine, Ph.D. thesis, Univ. of Paris-Est, Paris, France.

Joly, M., A. Voldoire, H. Douville, P. Terray, and J. F. Royer (2007), African monsoon teleconnections with tropical SSTs: validation and evolution in a set of IPCC4 simulations, Clim. Dyn., 29(1), 1–20.

Joly, M., and A. Voldoire (2009), Influence of ENSO on the West African monsoon: temporal aspects and atmospheric processes, J. Clim., 22(12), 3193–3210.

Kim, H. M., P. J. Webster, and J. A. Curry (2012), Evaluation of short-term climate change prediction in multi-model CMIP5 decadal hindcasts, Geophys. Res. Lett., doi:10.1029/2012GL051644.

Kirtman, B., S. B. Power, J. A. Adedoyin, G. J. Boer, R. Bojariu, I. Camilloni, F. J. Doblas-Reyes, A. M. Fiore, M. Kimoto, G. A. Meehl, M. Prather, A. Sarr, C. Schär, R. Sutton, G. J. van Oldenborgh, G. Vecchi and H. J. Wang (2013), Near-term Climate Change: Projections and Predictability, in Climate Change 2013: The Physical Science Basis, Contribution of Working Group I to the Fifth Assessment Report of the Intergovernmental Panel on Climate Change [Stocker, T.F., D. Qin, G.-K. Plattner, M. Tignor, S.K. Allen, J. Boschung, A. Nauels, Y. Xia, V. Bex and P.M. Midgley (eds.)], pp 953–1028, Cambridge University Press, Cambridge, United Kingdom and New York, NY, USA.

Knight, J. R., C. K. Folland, and A. A. Scaife (2006), Climate impacts of the Atlantic Multidecadal Oscillation, Geophys. Res. Lett., 33, doi:10.1029/2006GL026242.

Krishnan, R., and M. Sugi (2003), Pacific decadal oscillation and variability of the Indian summer monsoon rainfall, Clim. Dyn., 21(3–4), 233–242.

Kucharski, F., F. Molteni, M. P. King, R. Farneti, I. S. Kang, and L. Feudale (2013), On the need of intermediate complexity general circulation models: a ”SPEEDY” example, Bull. Amer. Meteor. Soc., 94, 25–30, doi: 10.1175/BAMS-D-11-00238.1.

Losada, T., B. Rodríguez-Fonseca, S. Janicot, S. Gervois, F. Chauvin, and P. Ruti (2010), A multi-model approach to the Atlantic Equatorial mode: impact on the West African monsoon, Clim. Dyn., 35, 29–43, doi:10.1007/s00382-009-0625-5.

MacDonald, G. M., and R. A. Case (2005), Variations in the Pacific Decadal Oscillation over the past millennium, Geophys. Res. Lett., 32(8).

Mantua, N. J., S. R. Hare, Y. Zhang, J. M. Wallace, and R. C. Francis (1997), A Pacific interdecadal climate oscillation with impacts on salmon production, Bull. Am. Meteorol. Soc., 78, 1069–1079.

Mantua, N. J., and S. R. Hare (2002), The Pacific Decadal Oscillation, J. Oceanogr., 58, 35–44.

Martin, E. R., C. Thorncroft, and B. B. B. Booth (2014), The Multidecadal Atlantic SST-Sahel Rainfall Teleconnection in CMIP5 Simulations, J. Clim., 27, 784–806, doi:10.1175/JCLI-D-13-00242.1.

Meehl, G. A., and A. Hu (2006), Megadroughts in the Indian monsoon region and southwest North America and a mechanism for associated multidecadal Pacific sea surface temperature anomalies, J. Clim., 19(9), 1605–1623.

Meehl, G. A., A. Hu, and B. D. Santer (2009), The mid-1970s climate shift in the Pacific and the relative roles of forced versus inherent decadal variability, J. Clim., 22, 780–792.

Meehl, G. A., A. Hu, J. M. Arblaster, J. Fasullo, and K. E. Trenberth (2013), Externally forced and internally generated decadal climate variability associated with the Interdecadal Pacific Oscillation, J. Clim., 26(18), 7298–7310.

Minobe, S. (1999), Resonance in bidecadal and pentadecadal climate oscillations over the North Pacific: Role in climatic regime shifts, Geophys. Res. Lett., 26, 855–858.

Mitchel, T. D., and P. D. Jones (2005), An improved method of constructing a database of monthly climate observations and associated high-resolution grids, Int. J. Climatol., 25, 693–712, doi:10.1002/joc.1181.

Mohino, E., S. Janicot, and J. Bader (2011a), Sahel rainfall and decadal and multi-decadal sea surface temperature variability, Clim. Dyn., 37, 419–440, doi:10.1007/s00382-010-0867-2.

Mohino, E., B. Rodríguez-Fonseca, C. R. Mechoso, S. Gervois, P. Ruti and F. Chauvin (2011b), Impacts of the Tropical Pacific/Indian Oceans on the Seasonal Cycle of the West African Monsoon, J. Clim., 24, 3878–3891 doi:10.1175/2011JCLI3988.1.

Molion, L. C. B., and P. S. Lucio (2013), A Note on Pacific Decadal Oscillation, El Nino Southern Oscillation, Atlantic Multidecadal Oscillation and the Intertropical Front in Sahel, Africa, Atmos. Clim. Sci., 3, doi:10.4236/acs.2013.33028.

Newman, M., G. P. Compo, and M. A. Alexander (2003), ENSO-forced variability of the Pacific decadal oscillation, J. Clim., 16(23), 3853–3857.

Newman, M. (2013), An empirical benchmark for decadal forecasts of global surface temperature anomalies, J. Clim., 26(14), 5260–5269.

Nicholson, S. E. (2013), The West African Sahel: A review of recent studies on the rainfall regime and its interannual variability, ISRN Meteorol, 2013, 453521.

van Oldenborgh, G. J., F. J. Doblas-Reyes, B. Wouters, and W. Hazeleger (2012), Decadal prediction skill in a multi-model ensemble, Clim. Dyn., 38, 1263–1280.

Power, S., T. Casey, C. Folland, A. Colman, and V. Mehta (1999), Inter-decadal modulation of the impact of ENSO on Australia, Clim. Dyn., 15, 319–324.

Rayner, N. A., D. E. Parker, E. B. Horton, C. K. Folland, L. V. Alexander, and D. P. Rowell (2003), Global analyses of sea surface temperature, sea ice, and night marine air temperature since the nineteenth century, J. Geophys. Res., 108. doi:10.1029/2002JD002670.

Rodríguez-Fonseca, B., S. Janicot, E. Mohino, T. Losada, J. Bader, C. Caminade, F. Chauvin, B. Fontaine, J. García-Serrano, S. Gervois, M. Joly, I. Polo, P. Ruti, P. Roucou, and A. Voldoire (2011), Interannual and decadal SST forced responses of the West African monsoon, Atmos. Sci. Lett., 12, 67–74, doi: 10.1002/ASL.308.

Schneider, N., and B. D. Cornuelle (2005), The Forcing of the Pacific Decadal Oscillation*, J. Clim., 18(21), 4355–4373.

Shakun, J. D., and J. Shaman (2009), Tropical origins of North and South Pacific decadal variability, Geophys. Res. Lett., 36(19), doi:10.1029/2009GL040313.

Shen, C., W. C. Wang, W. Gong, and Z. Hao (2006), A Pacific Decadal Oscillation record since 1470 AD reconstructed from proxy data of summer rainfall over eastern China, Geophys. Res. Lett., 33, doi:10.1029/2005GL024804.

Smith, T. M., R. W. Reynolds, T. C. Peterson, and J. Lawrimore (2008), Improvements to NOAA's historical merged land-ocean surface temperature analysis (1880–2006), J. Clim., 21, 2283–2296, doi:10.1175/2007JCLI2100.1.

Sultan, B., and S. Janicot (2003), The West African monsoon dynamics. Part II: The "preonset'" and "onset" of the summer monsoon, J. Clim., 16, 3407–3427.

Taylor, K. E., R. J. Stouffer, and G. A. Meehl (2012), An overview of CMIP5 and the experiment design, Bull. Amer. Meteor. Soc., 93, 485–498.

Ting, M., Y. Kushnir, R. Seager, and C. Li (2009), Forced and internal 20th century SST trends in the North Atlantic, J. Clim., 22, 1469–1481.

Ting, M., Y. Kushnir, R. Seager, and C. Li (2011), Robust features of Atlantic multi-decadal variability and its climate impacts, Geophys. Res. Lett., 38(17), doi:10.1029/2011GL048712.

Ting, M., Y. Kushnir, R. Seager, and C. Li (2014), North Atlantic Multidecadal SST Oscillation: External forcing versus internal variability, J. Mar. Sys., 133, 27–38.

Tourre, Y. M., B. Rajagopalan, Y. Kushnir, M. Barlow, and W. B. White (2001), Patterns of coherent decadal and interdecadal climate signals in the Pacific Basin during the 20th century, Geophys. Res.

Lett., 28(10), 2069–2072.

Trenberth, K. E., and J. W. Hurrell (1994), Decadal atmosphere-ocean variations in the Pacific, Clim. Dyn., 9, 303–319.

Vizy, E. K., K. H. Cook, J. Crétat, and N. Neupane (2013) Projections of a Wetter Sahel in the Twenty-First Century from Global and Regional Models, J. Clim., 26(13), 4664–4687.

Wang, X., A. S. Auler, R. L. Edwards, H. Cheng, E. Ito, Y. Wang, X. Kong, and M. Solheid (2007), Millennial-scale precipitation changes in southern Brazil over the past 90,000 years, Geophys. Res. Lett., 34(23).

Zeng, N., J. D. Neelin, K. M. Lau, and C. J. Tucker (1999), Enhancement of interdecadal climate variability in the Sahel by vegetation interaction, Science, 286, 1537–1540.

Zhang, Y., J. M. Wallace, and D. S. Battisti (1997), ENSO-like interdecadal variability: 1900-93, J. Clim., 10(5), 1004-1020.

Zhang, R., and T. L. Delworth (2006), Impact of Atlantic multidecadal oscillations on India/Sahel rainfall and Atlantic hurricanes, Geophys. Res. Lett., 33, doi:10.1029/2006GL026267.

Figure captions:

Figure 1. (a) Standardized IPO index obtained with ERSSTv3 from 1901-2008 as defined in the text. **(b)** IPO SST pattern defined as the regression of the unfiltered ERSSTv3 SSTA onto the standardized IPO index (units are K per standard deviation). **(c)** Regression map of unfiltered

CRUTS2.1 JAS precipitation anomaly onto the standardized IPO index (units are mm/day per standard deviation). Grey contours in (**b)** and **(c)** indicate the regions where the correlation is significant with a significance level of 0.05 (from a t-test).

Figure 2. Regression onto the IPO index of the unfiltered **(a)** SSTA (K per std. dev.) and **(b)** JAS precipitation anomalies (mm/day per std. dev.) averaged over the 17 CMIP5 models in the historical run, typically from 1850-2005 (details in Table S1). **(c)** and **(d)** same as **(a)** and **(b)** but for the piControl run. Black and grey marks indicate points where the regression coefficient sign coincides in at least 13 and 15 out of the 17 models analyzed, respectively. Grey contours indicate the regions where the averaged correlation is significant at alpha=0.05 (using a Monte Carlo-based test, see details in the supplementary material).

Figure 3. (a) Bar chart of correlation coefficient between IPO index and the unfiltered time series of the precipitation anomaly averaged over Sahel (between 17º-10ºN and 10ºW-10ºE, see box in Figure 2b) for the ensemble-mean historical simulations and observations (green) and piControl runs (yellow). The stems indicate the correlation threshold for statistical significance at alpha=0.05 (using a Monte Carlo-based test, see details in the supplementary material). (**b)** Scatter plot of the regression coefficient of precipitation anomaly over Sahel (between 17º-10ºN and 10ºW-10ºE, see box in Figure 2b) (units are mm/day per std. dev.), and the Tropical Pacific (15ºN-15ºS and 180º-95ºW, see box over the Pacific in Figure 2a) SSTA (units are K per std. dev.). The regression line fitted to all the points has a correlation coefficient R=-0.51. Numbers from 1 to 17 correspond to single models; 18 and 19 correspond to observations.

Figure 4. (a) Regression of the unfiltered JAS anomaly of velocity potential at 200 hPa from 20th Century Reanalysis (1901-2008) onto the IPO index; **(b)** and **(c)** same as **(a)** but for the averaged regression in the historical and piControl simulations, respectively; **(d)**, **(e)** and **(f)** same as **(a)**, **(b)**

and **(c)** but for the velocity potential at 850 hPa (10^6 m^2/s per std. dev.). Vectors represent the divergent wind; in black at points where the sign of the regression coefficient of the velocity potential coincides in at least 15 out of the 17 models analyzed and in grey at the rest of the points in **(b)**, **(c)**, **(e)** and **(f)**. Grey contours indicate the regions where the averaged correlation is significant at alpha=0.05 (using a Monte Carlo-based test, see details in the supplementary material).

Figure 5. Regression onto the IPO index of the unfiltered **(a)** SSTA (K per std. dev.) and **(b)** JAS precipitation anomalies (mm/day per std. dev.) averaged over the 17 CMIP5 models in the rcp8.5 run, typically from 2006-2100 (details in Table S1). Black and grey marks indicate points where the regression coefficient sign coincides in at least 13 and 15 out of the 17 models analyzed, respectively. Grey contours indicate the regions where the averaged correlation is significant at alpha=0.05 (using a Monte Carlo-based test, see details in the supplementary material).

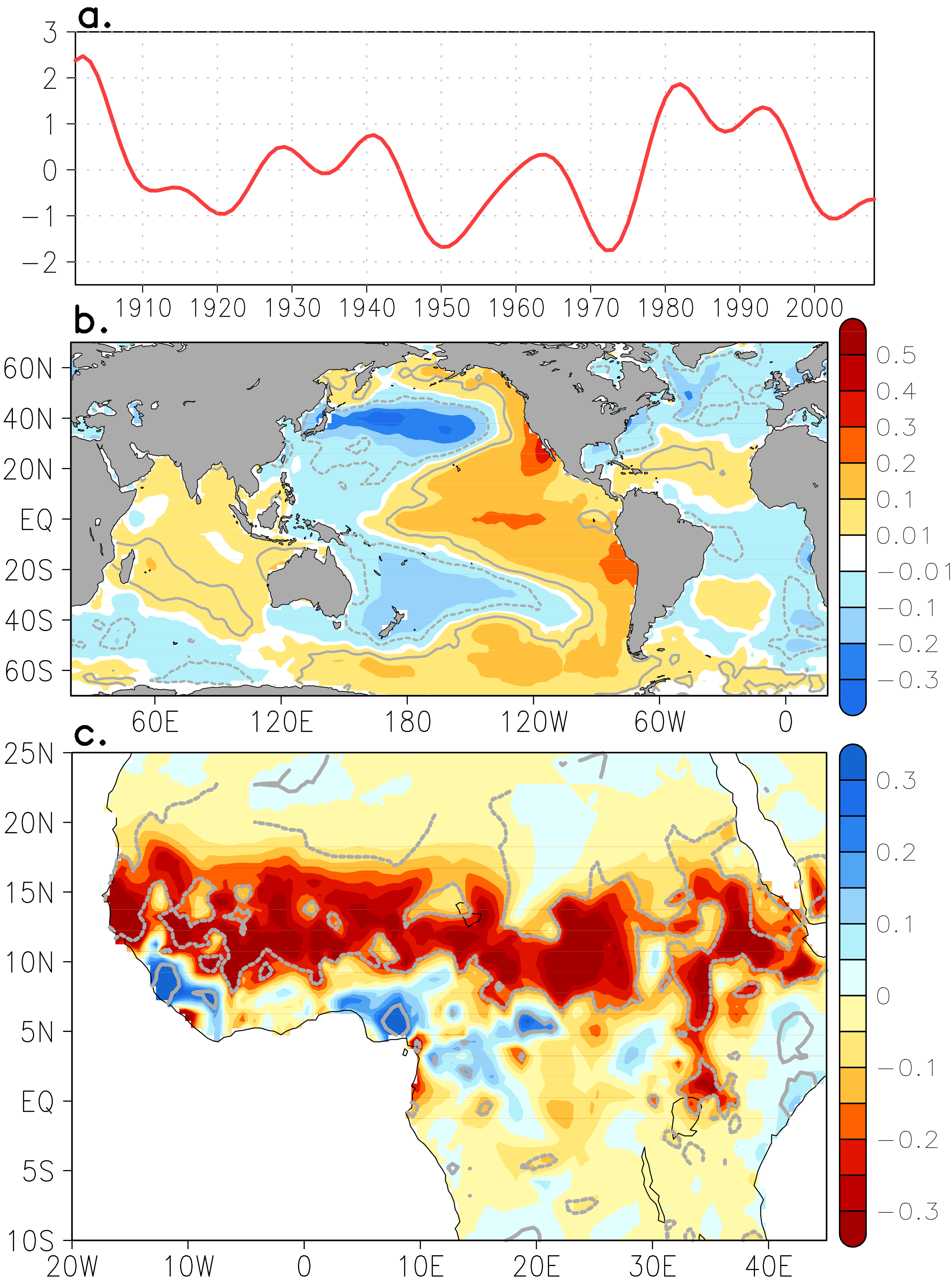

a.
3
2
1
0
−1
−2
1910 1920 1930 1940 1950 1960 1970 1980 1990 2000
b.
60N
40N
20N
EQ
20S
40S
60S
60E 120E 180 120W 60W 0
0.5
0.4
0.3
0.2
0.1
0.01
−0.01
−0.1
−0.2
−0.3
c.
25N
20N
15N
10N
5N
EQ
5S
10S
20W 10W 0 10E 20E 30E 40E
0.3
0.2
0.1
0
−0.1
−0.2
−0.3

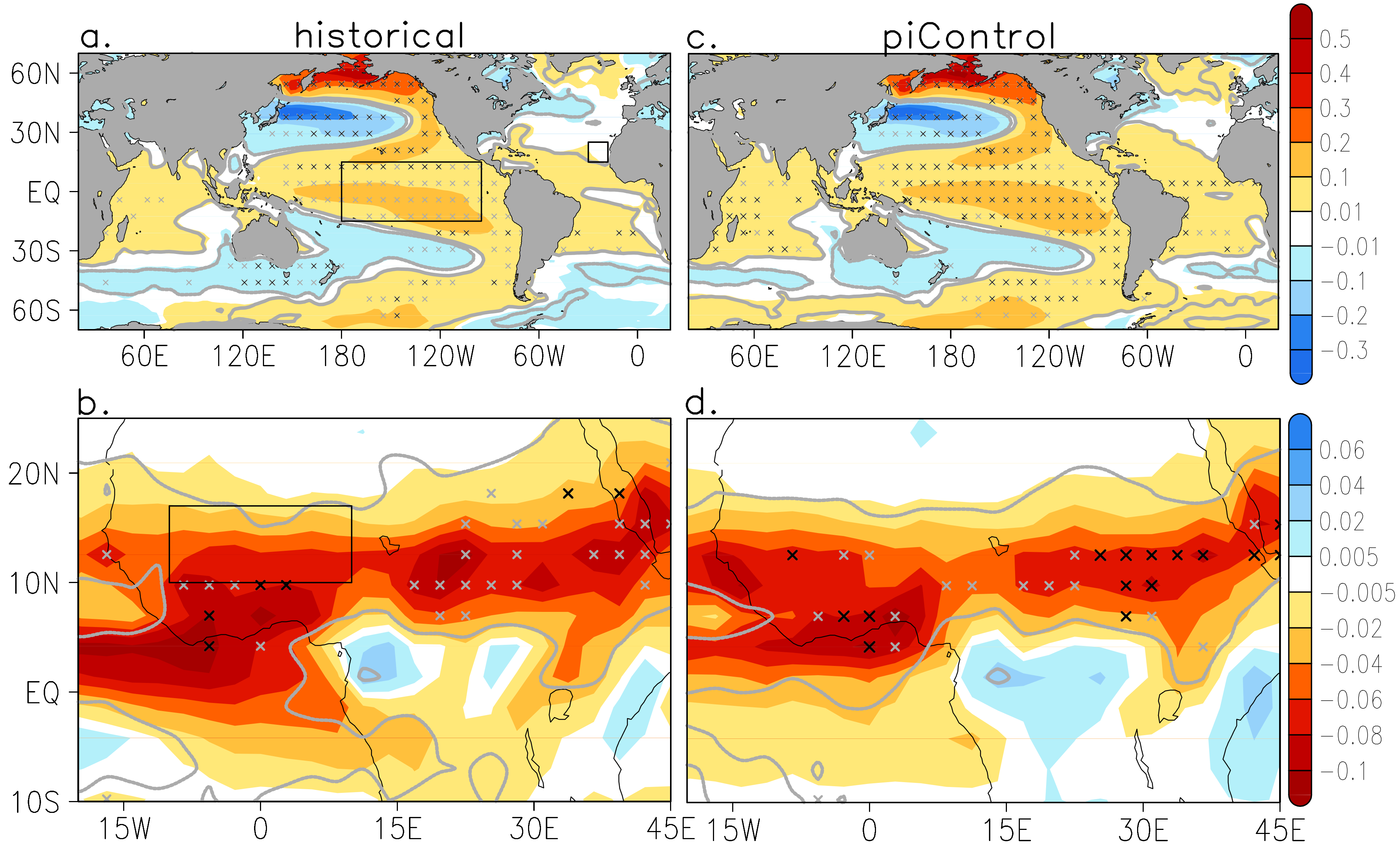
a.
historical
c.
piControl
60N
30N
EQ
30S
60S
60E
120E
180
120W
60W
0
0.5
0.4
0.3
0.2
0.1
0.01
−0.01
−0.1
−0.2
−0.3
b.
d.
20N
10N
EQ
10S
15W
0
15E
30E
45E
0.06
0.04
0.02
0.005
−0.005
−0.02
−0.04
−0.06
−0.08
−0.1

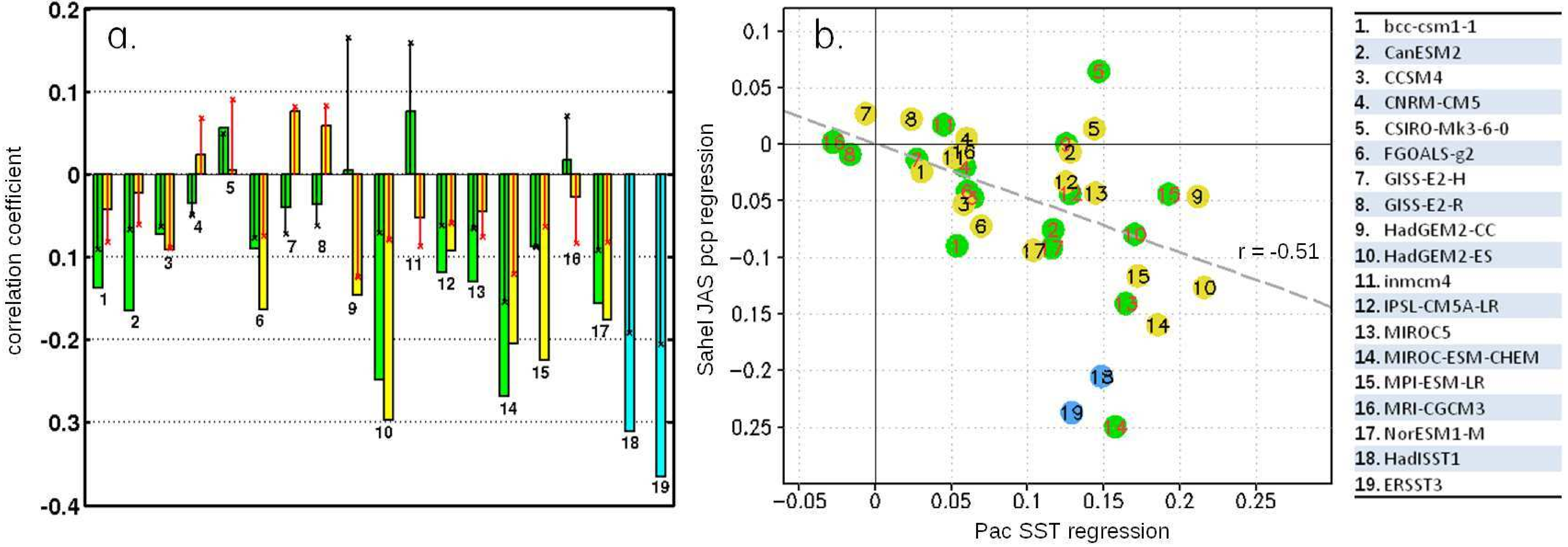

a.
correlation coefficient
b.
Sahel JAS pcp regression
Pac SST regression
r = -0.51
1. bcc-csm1-1
2. CanESM2
3. CCSM4
4. CNRM-CM5
5. CSIRO-Mk3-6-0
6. FGOALS-g2
7. GISS-E2-H
8. GISS-E2-R
9. HadGEM2-CC
10. HadGEM2-ES
11. inmcm4
12. IPSL-CM5A-LR
13. MIROC5
14. MIROC-ESM-CHEM
15. MPI-ESM-LR
16. MRI-CGCM3
17. NorESM1-M
18. HadISST1
19. ERSST3

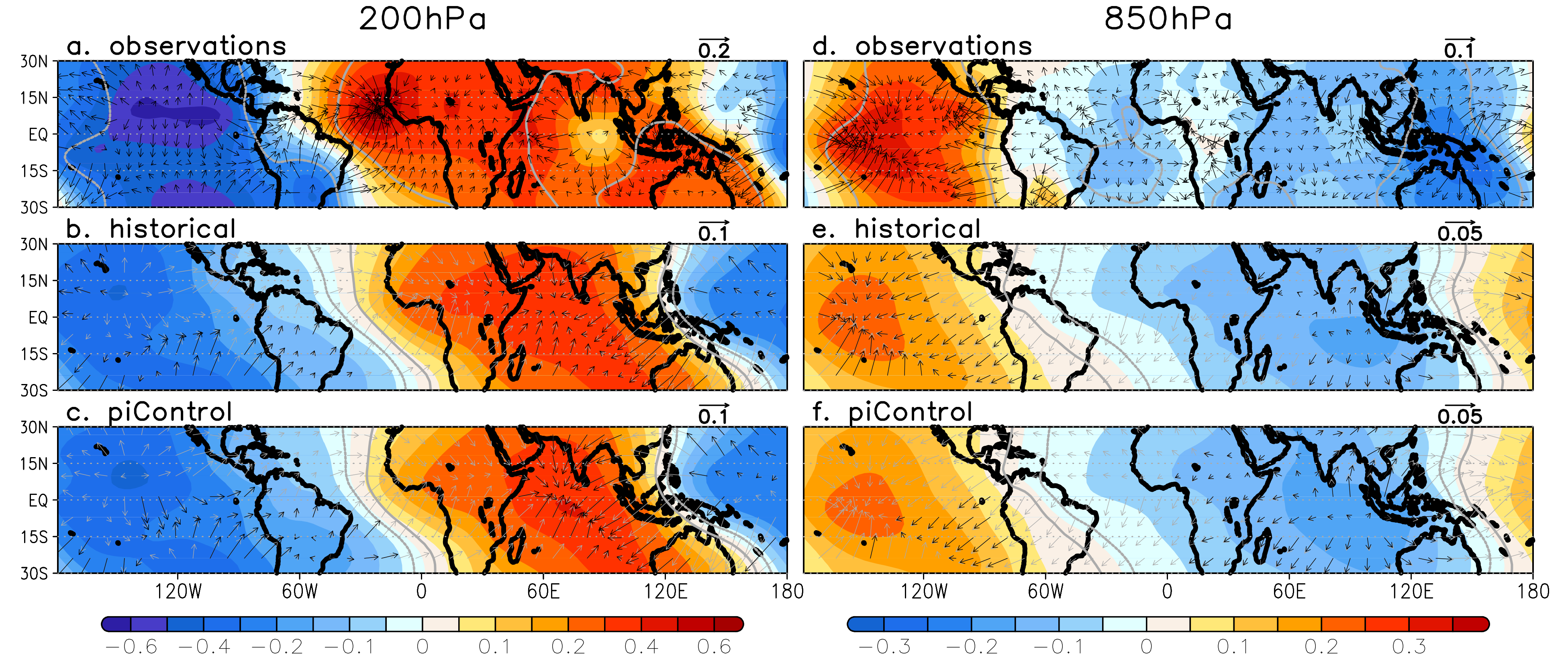
200hPa
850hPa
a. observations
b. historical
c. piControl
d. observations
e. historical
f. piControl
0.2
0.1
0.1
0.1
0.05
0.05
30N
15N
EQ
15S
30S
120W
60W
0
60E
120E
180
−0.6
−0.4
−0.2
−0.1
0
0.1
0.2
0.4
0.6
−0.3
−0.2
−0.1
0
0.1
0.2
0.3

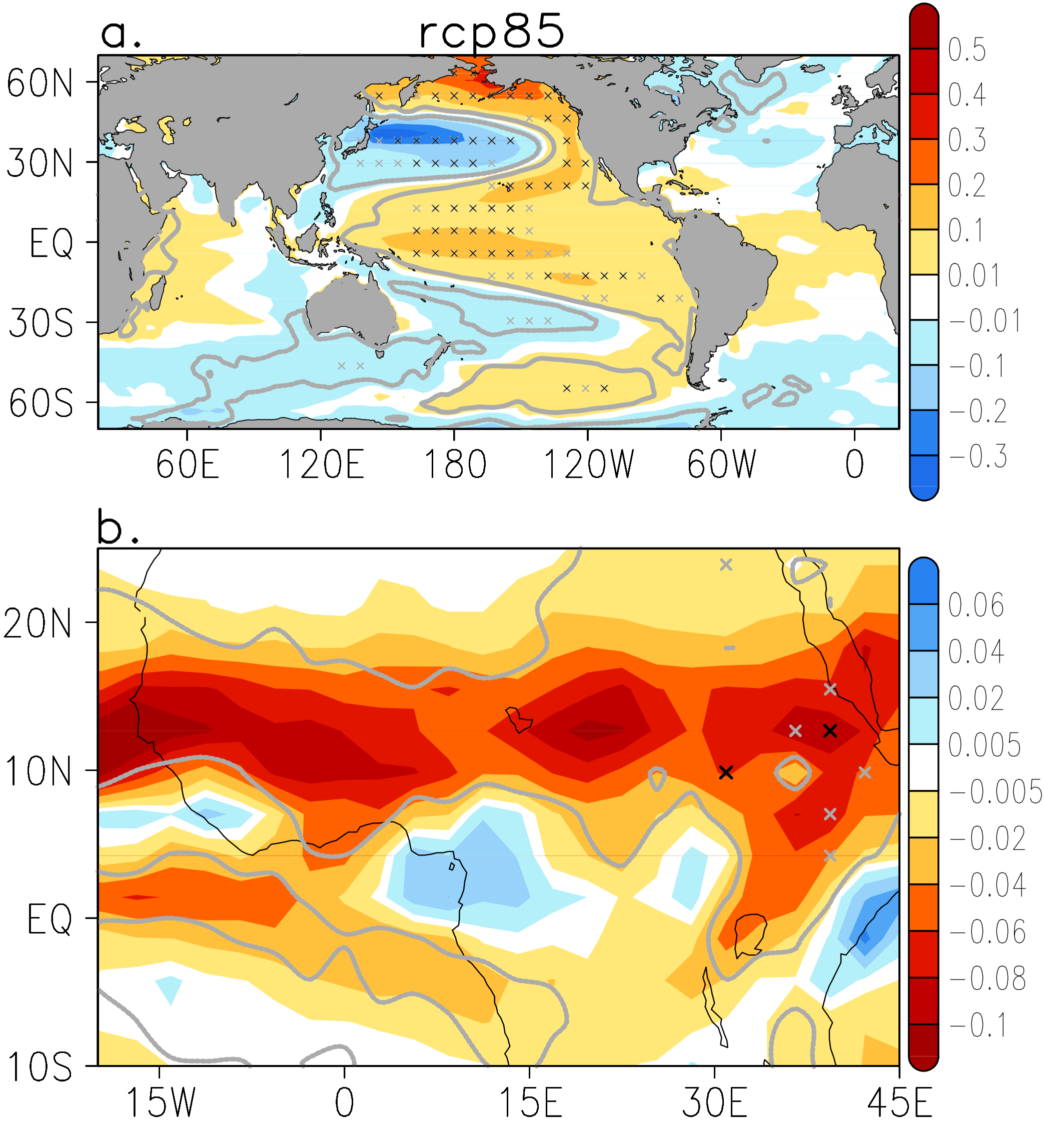
a.
rcp85
60N
30N
EQ
30S
60S
60E
120E
180
120W
60W
0
0.5
0.4
0.3
0.2
0.1
0.01
−0.01
−0.1
−0.2
−0.3
b.
20N
10N
EQ
10S
15W
0
15E
30E
45E
0.06
0.04
0.02
0.005
−0.005
−0.02
−0.04
−0.06
−0.08
−0.1

Auxiliary material for: 2014GL062473

Robust Sahel drought due to the Interdecadal Pacific Oscillation in CMIP5 simulations.

Julián Villamayor[1] and Elsa Mohino[2]

Affiliation:

[1,2]Departamento de Física de la Tierra, Astronomía y Astrofísica I, Universidad Complutense de Madrid, Madrid, Spain.

Contact:

[1]Av. Complutense s/n, 28040 Madrid, Spain. julian.villamayor@fis.ucm.es

[2]Av. Complutense s/n, 28040 Madrid, Spain. emohino@fis.ucm.es

1. Information relating to the Monte Carlo-based test used to determine the significance of the model-mean regression maps:

A Monte Carlo test is used to test the regression maps averaged across the 17 models by comparing the averaged correlation against a probability density function. This density function is constructed from mean correlations out of 17 pairs of random time series. The length of these time series is the number of years times the number of realizations available of each of the 17 models (see Table S1), since we analyze the data of the models with several realizations available concatenated in time. For each correlated pair, one random time series is 13-year lowpass-filtered and the other is not, similarly to what we do when regress the IPO filtered indices onto the unfiltered anomaly fields to feature the spatial patterns. We repeat the process 1000 times to build the probability density function against which the original mean regression is compared.

2. Supplementary table and figures that may be useful to better follow the article:

		piControl	historical		rcp8.5	
		#yrs	#yrs	#rea	#yrs	#rea
1	bcc-csm1-1	500	163*	3	95	1
2	CanESM2	996	156	5	95	5
3	CCSM4	501	156	6	95	6
4	CNRM-CM5	850	156	10	95	5
5	CSIRO-Mk3-6-0	500	156	10	95	10
6	FGOALS-g2	700	156	4	95	1
7	GISS-E2-H	540	156	5	95	5
8	GISS-E2-R	550	156	6	95	5
9	HadGEM2-CC	240	145**	1	94***	3
10	HadGEM2-ES	575	145**	5	95	4
11	inmcm4	500	156	1	95	1
12	IPSL-CM5A-LR	1000	156	6	95	4
13	MIROC5	670	163*	5	95	3
14	MIROC-ESM-CHEM	255	156	1	95	1
15	MPI-ESM-LR	1000	156	3	95	3
16	MRI-CGCM3	500	156	5	95	1
17	NorESM1-M	501	156	3	95	1

Table S1. List of CMIP5 models analyzed, number of years (#yrs) and realizations (#rea) of each simulation. The historical experiment are simulations of the period 1850-2005 (exceptions are 1850-2012 (*) and 1860-2004 (**)). The rcp8.5 simulation period is 2006-2100 (exception is 2006-2099(***)). All data are available at http://pcmdi9.llnl.gov.

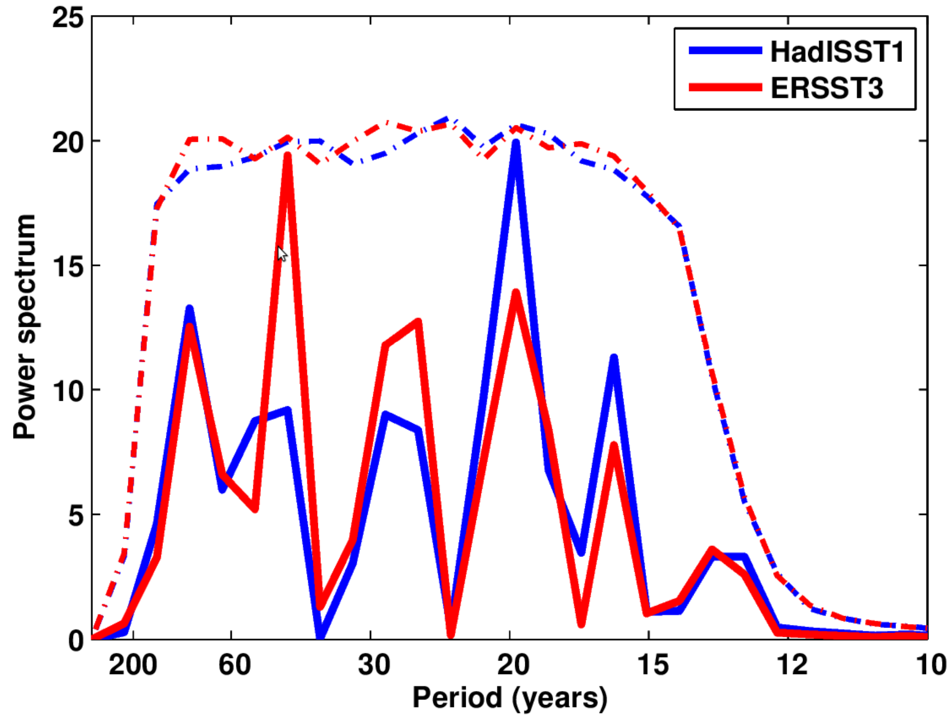

Figure S1. Power spectrum of the Fourier transform of the detrended IPO indices from observations. Dashed lines indicate the 95% confidence level following a Monte Carlo-based test in which a probability density is built from the Fourier spectrum of 13-year lowpass-filtered and detrended white noise time series.

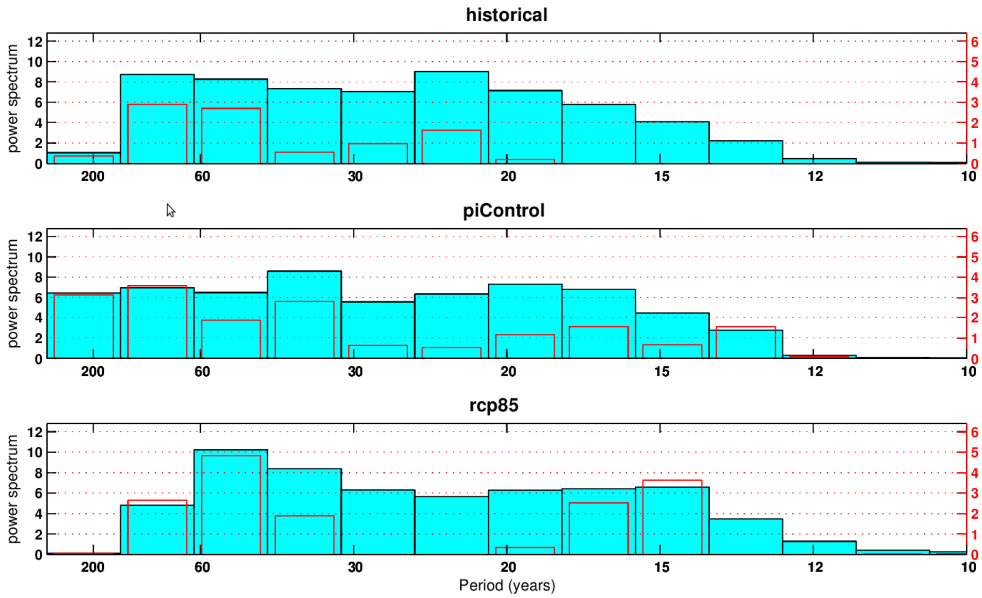

Figure S2. Model-mean power spectra of the Fourier transform of the detrended IPO indices (blue bars) of the historical (top), piControl (middle) and rcp8.5 simulations (bottom). Red bars indicate the power spectra averaged over the 17 models but taking into account only 95% significant peaks for each of them. The statistical significance for each model's IPO is obtained following a Monte Carlo-based test in which a probability density function is built from the Fourier spectrum of 13-year lowpass-filtered and detrended white noise time series with the same time length as the simulation and averaged across the number of ensemble members in cases where more than one realization is available.

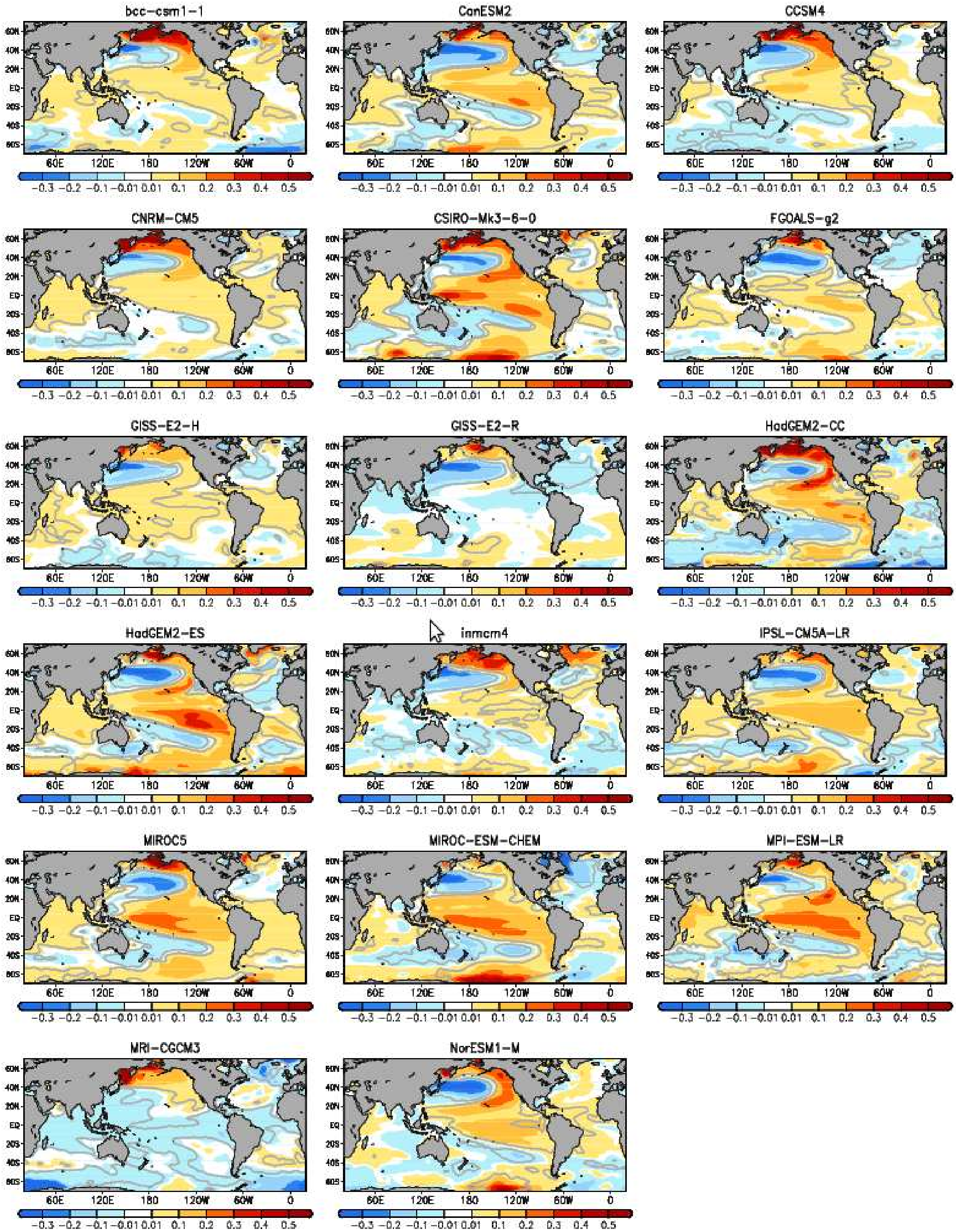

Figure S3. Single models IPO SST patterns from historical simulations defined as the regression of the SSTA onto the standardized IPO index (units are K per standard

deviation). Grey contours indicate the regions where the correlation is significant with a significance level of 0.05 (from a t-test).

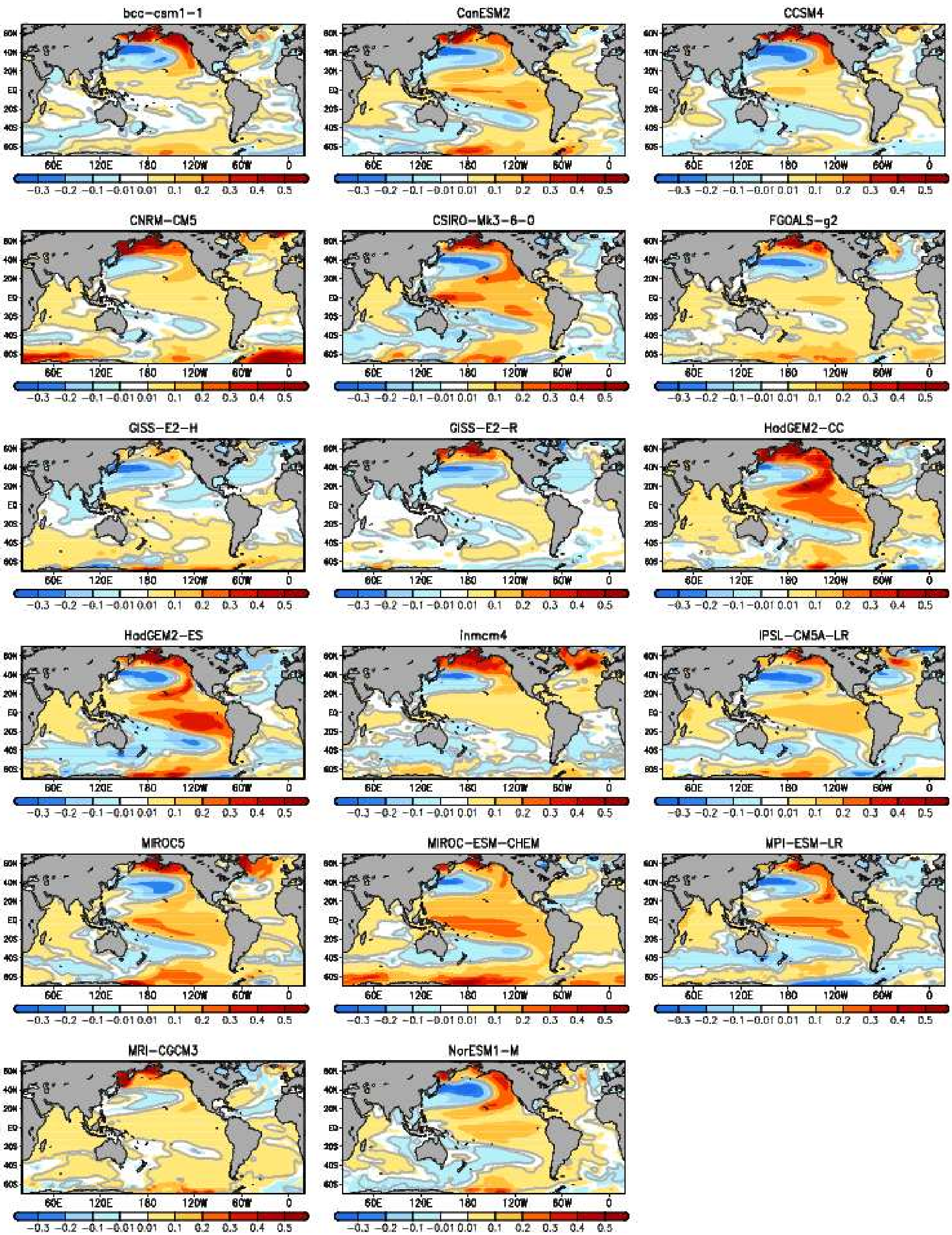

Figure S4. Single models IPO SST patterns from piControl simulations defined as the regression of the SSTA onto the standardized IPO index (units are K per standard

deviation). Grey contours indicate the regions where the correlation is significant with a significance level of 0.05 (from a t-test).

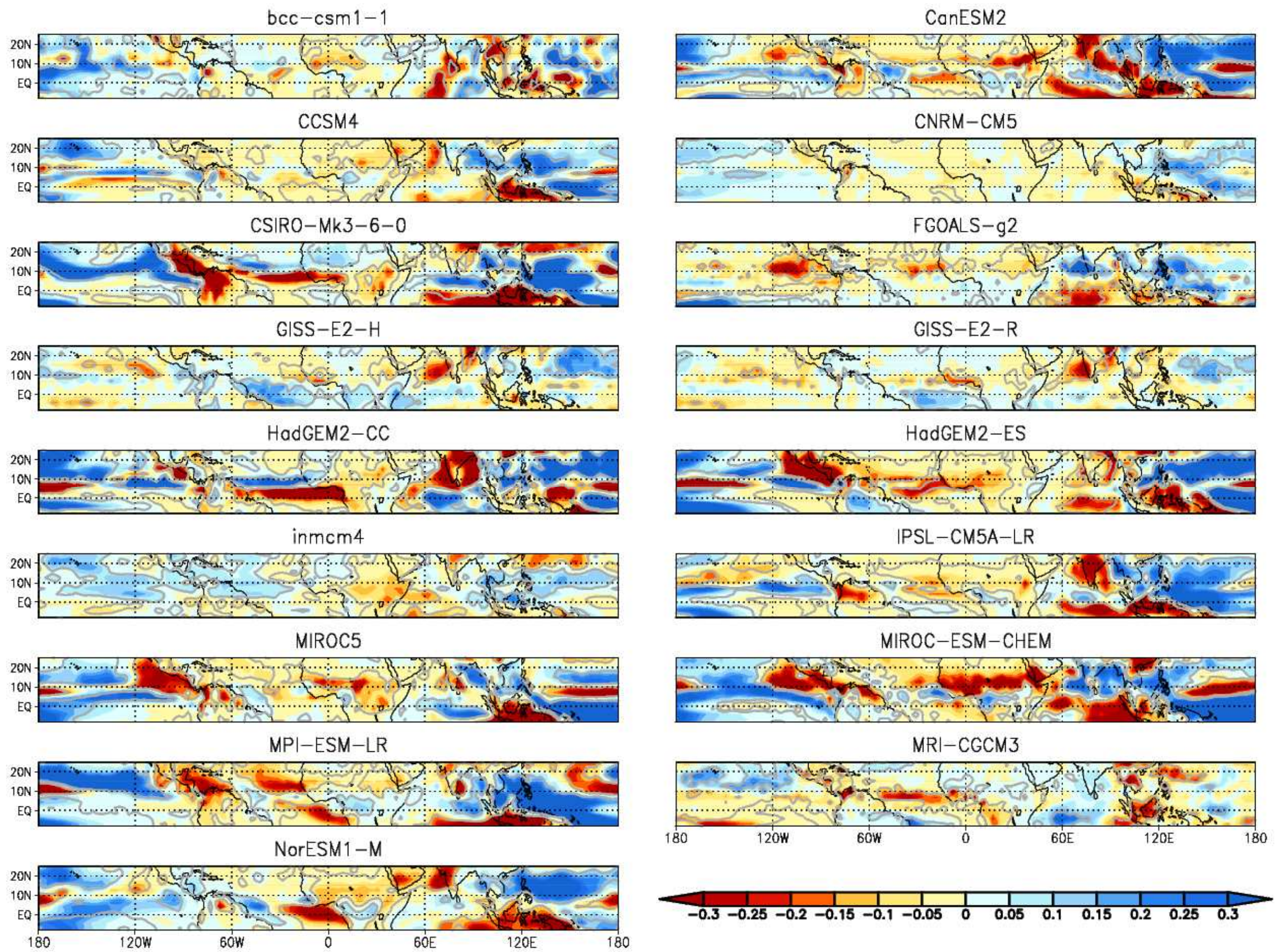

Figure S5. Single models regression maps of JAS precipitation anomalies onto the standardized IPO index (mm/day per std. dev.) from historical simulations. Grey contours indicate the regions where the correlation is significant with a significance level of 0.05 (from a t-test).

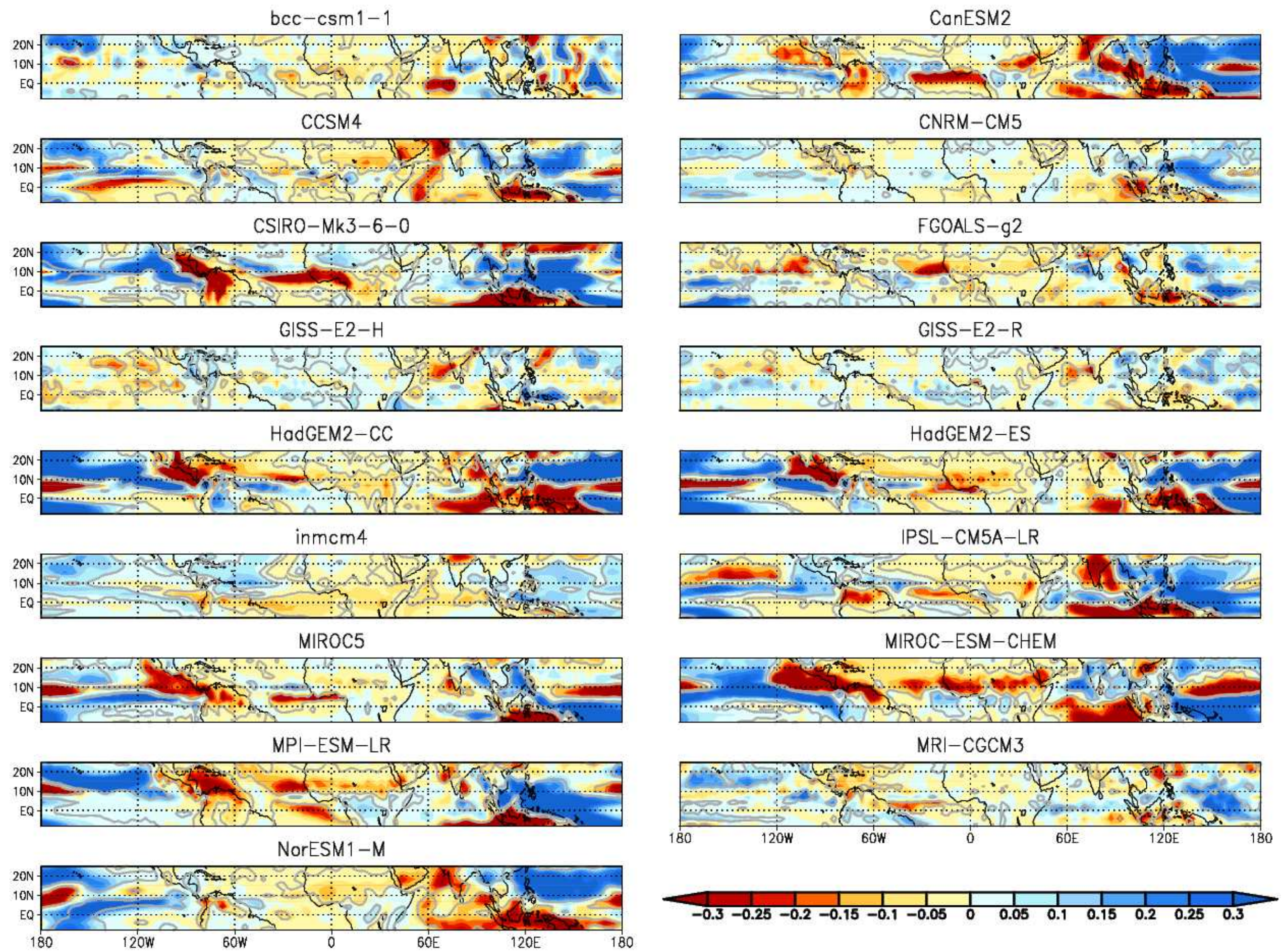

Figure S6. Single models regression maps of JAS precipitation anomalies onto the standardized IPO index (mm/day per std. dev.) from piControl simulations. Grey contours indicate the regions where the correlation is significant with a significance level of 0.05 (from a t-test).

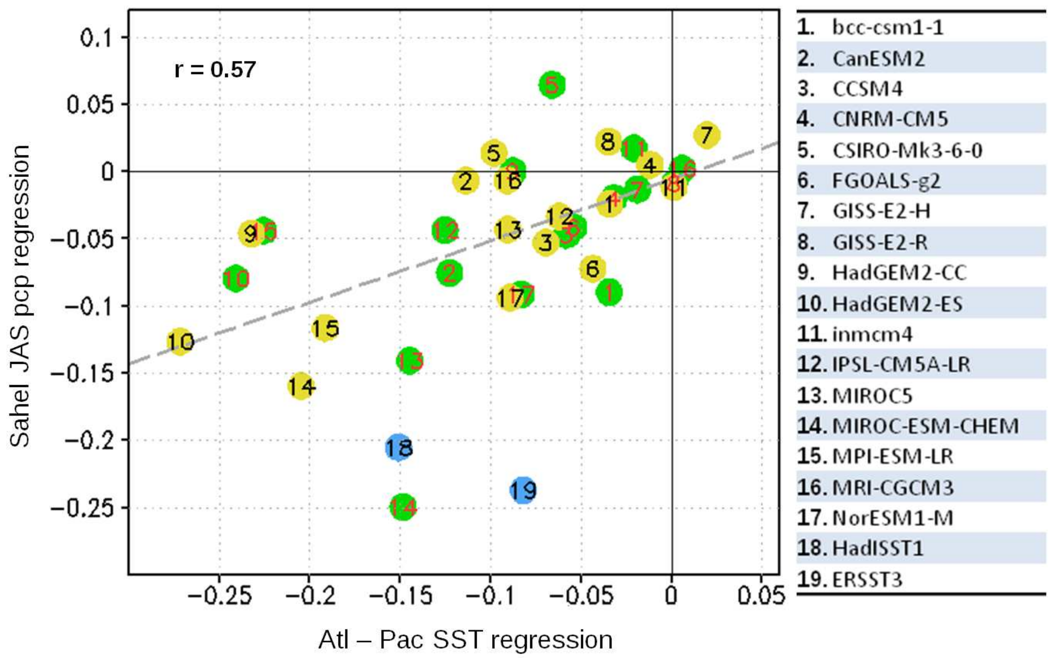

Figure S7. Scatter plot of the regression coefficient of precipitation anomaly over Sahel (between 17º-10ºN and 10ºW-10ºE, see box in Figure 2b) (units are mm/day per std. dev.), and the SSTA difference between the Tropical Atlantic coastal region next to West Africa (25º-15ºN and 30º-18ºW, see box over the Tropical Atlantic in Figure 2a) and the Tropical Pacific (15ºN-15ºS and 180º-95ºW, see box over the Tropical Pacific in Figure 2a) SSTA (units are K per std. dev.). The regression line fitted to all the points has a correlation coefficient R=0.57. Numbers from 1 to 17 correspond to single models; 18 and 19 correspond to observations.

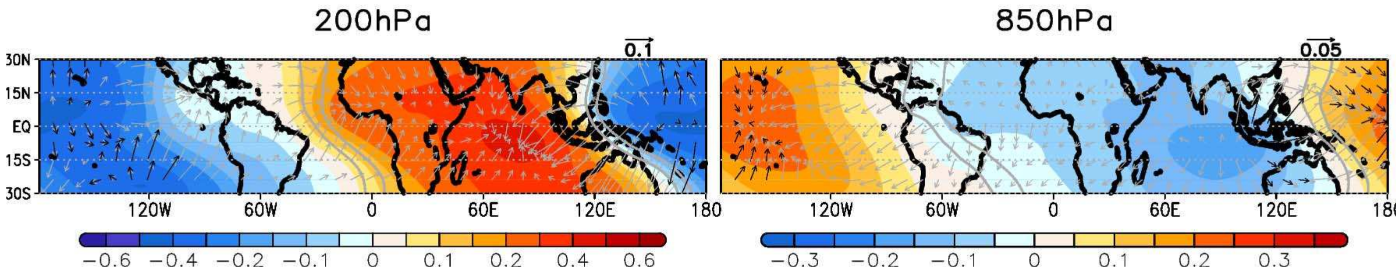

Figure S8. Averaged regression in the rcp8.5 simulation of the JAS anomaly of velocity potential at 200 hPa and 850 hPa onto the standardized IPO index (10^6 m^2/s per std. dev.). Divergent wind derived from this pattern is represented by black vectors at points where the sign of the regression coefficient of the velocity potential coincides in at least 15 out of the 17 models analyzed and by gray vectors at the rest of the points. Grey contours indicate the regions where the averaged correlation is significant at alpha=0.05 (using a Monte Carlo-based test, see details in the supplementary material).

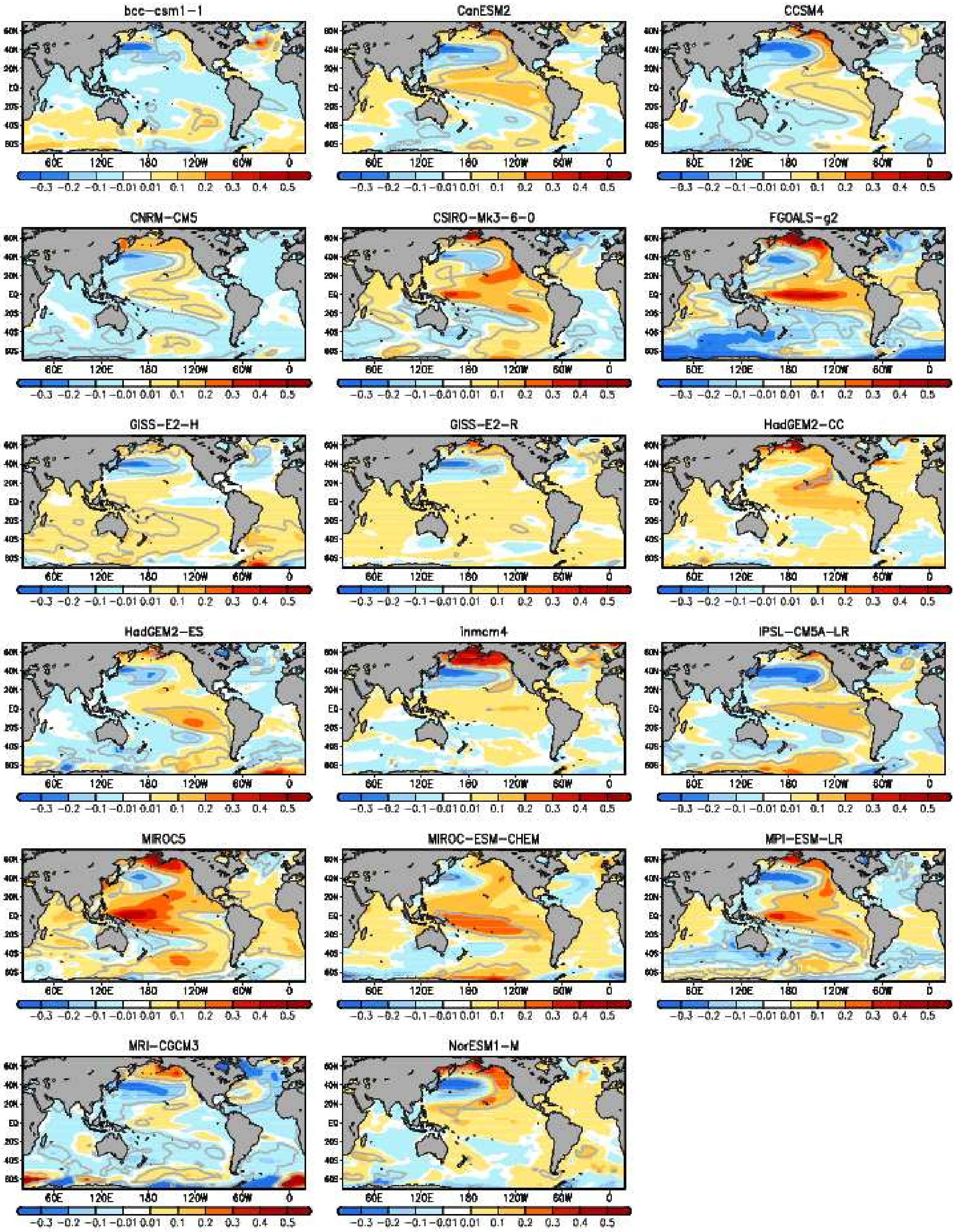

Figure S9. Single models IPO SST patterns from rcp8.5 simulations defined as the regression of the SSTA onto the standardized IPO index (units are K per standard

deviation). Grey contours indicate the regions where the correlation is significant with a significance level of 0.05 (from a t-test).

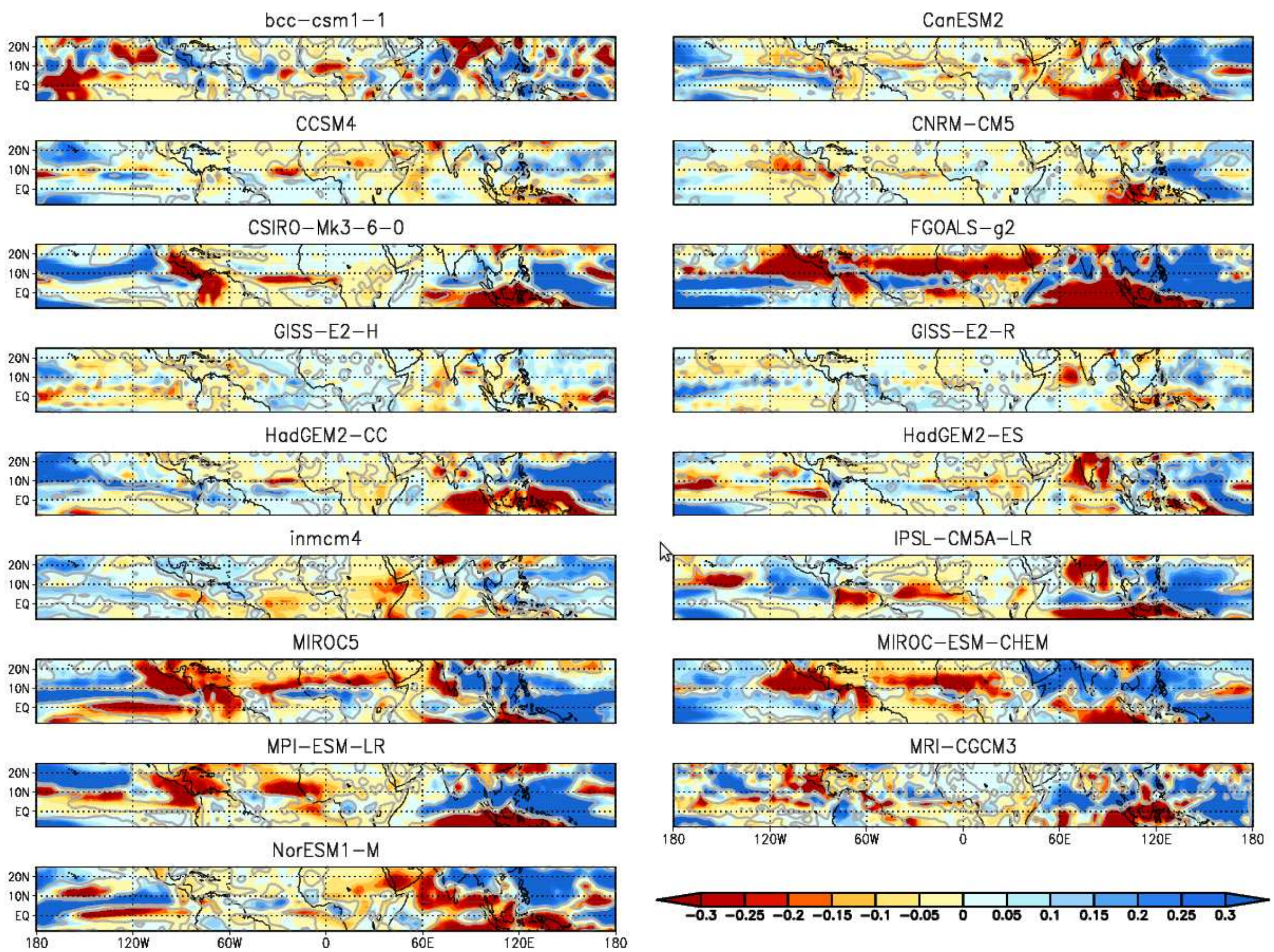

Figure S10. Single models regression maps of JAS precipitation anomalies onto the standardized IPO index (mm/day per std. dev.) from rcp8.5 simulations. Grey contours indicate the regions where the correlation is significant with a significance level of 0.05 (from a t-test).